

Article

Design of a Step-Up DC–DC Converter for Standalone Photovoltaic Systems with Battery Energy Storages

Yun-Gyeong Oh ¹, Woo-Young Choi ² and Jung-Min Kwon ^{1,*} 

¹ Department of Electrical Engineering, Hanbat National University, Daejeon 34158, Korea; 5yun5@naver.com

² Division of Electronic Engineering, Jeonbuk National University, Jeonju 54896, Korea; wychoi@jbnu.ac.kr

* Correspondence: jmkwon@hanbat.ac.kr

Abstract: This paper proposes a step-up DC–DC converter for a power electronic circuit for standalone photovoltaic systems with battery energy storages. The proposed DC–DC converter effectively converts low DC battery voltage into high DC-link voltage. It operates with soft-switching characteristics, which can reduce switching power losses. The proposed converter operates without output voltage feedback, which simplifies its control design. The operation principle of the proposed converter was described, along with the overall system configuration. The experimental results were discussed for the 500-W prototype system using a 12-V lead-acid battery.

Keywords: photovoltaic; stand-alone; step-up; converter; push-pull converter; resonant voltage doubler rectifier

1. Introduction

The standalone photovoltaic (PV) systems are widely used in the off-grid areas. In general, the standalone PV systems consist of photovoltaic panels, a maximum power point tracking (MPPT) charger, a battery energy storage, and a standalone inverter [1,2]. As shown in Figure 1, The MPPT charger extracts the maximum power from the PV panels and charges the battery. The battery stores excess power, which can be stably supplied to loads. A 12-V lead-acid battery is widely used since the lead-acid battery is relatively inexpensive and easy to handle. The standalone inverter has the intermediate DC–DC converter and the single-phase inverter. This inverter converts the low battery voltage into the sinusoidal AC output voltage.

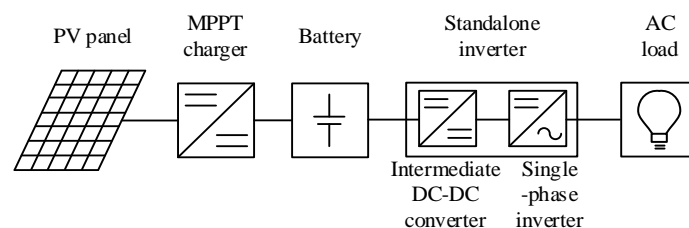


Figure 1. Configuration of the Standalone PV Systems.

In a typical standalone inverter, the full-bridge inverter is used with a bulky line-frequency transformer. However, the line-frequency transformer increases the cost and the size and lowers the overall power efficiency. In order to cope with these drawbacks, various types of DC–DC converters utilizing high-frequency transformers have been designed for the intermediate DC–DC converter [3,4]. These converters provide high power conversion efficiency along with the advantages of small size and light weight.

The current-fed DC–DC converters are suitable for the intermediate DC–DC converter, which has low input voltage and high current batteries. It has the advantages such as a low input current ripple, low conduction loss, high voltage conversion ratio, and reduced



Citation: Oh, Y.-G.; Choi, W.-Y.; Kwon, J.-M. Design of a Step-Up DC–DC Converter for Standalone Photovoltaic Systems with Battery Energy Storages. *Energies* **2022**, *15*, 44. <https://doi.org/10.3390/en15010044>

Academic Editor: Jelena Loncarski

Received: 23 November 2021

Accepted: 20 December 2021

Published: 22 December 2021

Publisher's Note: MDPI stays neutral with regard to jurisdictional claims in published maps and institutional affiliations.



Copyright: © 2021 by the authors. Licensee MDPI, Basel, Switzerland. This article is an open access article distributed under the terms and conditions of the Creative Commons Attribution (CC BY) license (<https://creativecommons.org/licenses/by/4.0/>).

transformer turns' ratio [5–8]. However, the current-fed converters have a boost inductor at the input terminal, which results in large size and high cost. In addition, they have high voltage spikes for power switches resulting from the stored energy at the boost inductor. On the other hand, the voltage-fed DC–DC converters have low primary switch voltage stress, minimal components, and small size [9–21]. The voltage-fed converters can be classified into the unidirectional core excitation topology and the bidirectional core excitation topology. The unidirectional core excitation topology such as flyback and forward converters has low magnetic core utilization since the magnetic flux is unbalanced and saturated [9]. Therefore, the unidirectional core excitation topology converters are used at low power level applications. Compared to the unidirectional core excitation converters, the bidirectional core excitation topology such as push–pull, half-bridge, and full-bridge converters have higher magnetic core utilization [10–13]. Therefore, the bidirectional core excitation topology converters are used for higher power level applications.

As a voltage-fed converter, the push–pull converter has desirable features for an intermediate DC–DC converter [13,14]. The push–pull converter has two power switches with a common ground, which can have simple gate-driving circuits. Additionally, it has a simple structure, galvanic isolation, and high voltage conversion ratio. If the soft switching is achieved, it has low switching losses, high efficiency, and improved electromagnetic interference.

Unfortunately, the major drawback of the push–pull converter is that the voltage stress of the switches is twice the input voltage. To reduce the switching losses, several topologies are proposed. The active clamp or auxiliary circuits are employed to absorb voltage spike and achieve soft switching [14,15]. However, it increases the components, control complexity, size, and cost of the designed converter. The resonant techniques are employed to suppress voltage spike [16–22], which provides the soft switching operation of power switches at the primary side. However, the switching power losses should be considered at the secondary side, where power diodes generate switching power losses during their switching operations.

This paper proposes a step-up DC–DC converter, which can effectively convert low battery voltage into high dc-link voltage for the standalone PV systems. As shown in Figure 2, the proposed step-up DC–DC converter consists of the push–pull converter and resonant voltage doubler rectifier. The resonant voltage doubler rectifiers provide a higher voltage conversion ratio and reduce the high turns' ratio in the transformer [16–22]. It operates in the discontinuous conduction mode (DCM) to reduce the switching losses and to remove the reverse-recovery losses for the power diodes at the secondary side. The primary switches operate under the zero-voltage switching (ZVS) operation. The diodes are turned off at zero current due to resonance between leakage inductance L_{lk} and resonant capacitors C_{r1} and C_{r2} . The proposed step-up DC–DC converter can operate with the open loop condition by removing the auxiliary circuits for the output voltage feedback control. To show the entire control strategy for the proposed step-up DC–DC converter, the overall PV standalone system was suggested. The 500-W prototype was implemented with minimal components. This paper is organized as follows. In Section 2, the step-up DC–DC converter is analyzed. Its operation principle (2.1) is described for the steady-state operation condition. Its design guidelines (2.2) are also presented for the high-frequency transformer and the resonant circuit components. In Section 3, the control strategy of the DC–DC converter is presented. The overall system configuration (3.1) is described. The detailed control schemes (3.2) for power electronic circuits are introduced. In Section 4, the experimental results are discussed for the 500-W prototype system. Twelve-V lead-acid batteries were utilized for battery energy storages. A step-down DC–DC converter converted the photovoltaic power into the battery power. Experimental results verified the effectiveness of the proposed DC–DC converter. Finally, Section 5 gives the concluding remarks.

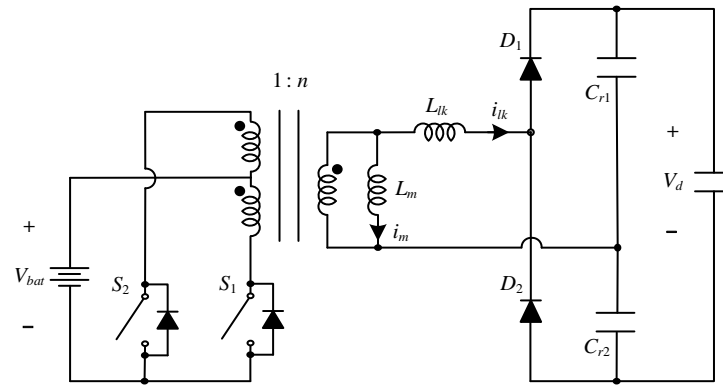


Figure 2. Proposed step-up DC–DC converter.

2. Proposed Converter

2.1. Operation Principle

The proposed step-up converter, as shown in Figure 2, consisted of the push–pull converter and the resonant voltage doubler rectifier. The switches S_1 and S_2 operated alternately with 50% duty of the switching cycle. The resonant voltage doubler rectifier was composed of the diodes D_1 and D_2 and resonant capacitors C_{r1} and C_{r2} . It was driven in the DCM to reduce current stress of the switches and achieve zero current turn off the diodes. The following assumptions were made for simplified analysis.

1. The switches S_1 and S_2 were ideal except for their body diodes D_{S1} and D_{S2} , respectively.
2. The high frequency transformer had a turn ratio $1:n$ and was modeled as the magnetizing inductances L_m and leakage inductance L_{lk} .
3. The output voltage of DC link V_d was constant because the DC link capacitor C_d was sufficiently large.
4. The resonant capacitors C_{r1} and C_{r2} had the equal capacity to operate symmetrically.

The proposed high step-up DC–DC converter was divided into six operation modes. Figures 3 and 4 show the three operation modes and their theoretical waveforms, respectively. Prior to *Mode 1*, the switch S_2 was turned on, allowing the current to flow slightly. The current i_{lk} across the leakage inductance L_{lk} was zero.

Mode 1 [t_0, t_1]: At t_0 , the switch S_2 was turned off with the current stress reduced. The voltage across switch S_2 was rapidly charged to twice the battery voltage V_{bat} . The drain–source current i_{S1} across switch S_1 discharged the drain–source voltage V_{S1} across switch S_1 to zero and flowed through the body diode D_{S1} . The magnetizing current i_m increased linearly as follows:

$$i_m(t) = i_m(t_0) + \frac{nV_{bat}(t - t_0)}{L_m} \quad (1)$$

Mode 2 [t_1, t_2]: At t_1 , the switch S_1 was turned on at zero voltage. The power was transferred to the DC link through the transformer. The inductance L_{lk} and resonant capacitors C_{r1} and C_{r2} resonated and the current i_{lk} flowed through the diode D_1 . The state equation can be written as follows:

$$L_{lk} \frac{di_{Llk}(t)}{dt} = nV_{bat} - v_{Cr1}(t) \quad (2)$$

$$V_d = v_{Cr1}(t) + v_{Cr2}(t) \quad (3)$$

$$i_{lk}(t) = C_{r1} \frac{dv_{Cr1}}{dt} - C_{r2} \frac{dv_{Cr2}}{dt} = C_r \frac{dv_{Cr1}}{dt} \quad (4)$$

where the resonant capacitor C_r is as:

$$C_r = C_{r1} + C_{r2} \quad (5)$$

From Equations (2)–(4), the voltage v_{cr1} across the resonant capacitor C_{r1} is derived as:

$$v_{cr1}(t) = nV_{bat} - [nV_{bat} - v_{cr1}(t_1)]\cos\omega_r(t - t_1) \quad (6)$$

Since the initial value of i_{lk} is zero, i_{lk} is obtained as:

$$i_{lk}(t) = \frac{nV_{bat} - v_{cr1}(t_1)}{Z_r}\sin\omega_r(t - t_1) = I_{lk, peak}\sin\omega_r(t - t_1) \quad (7)$$

where $I_{lk, peak}$ is the peak of i_{lk} . The impedance Z_r and the angular resonance frequency ω_r are written as follows:

$$Z_r = \sqrt{\frac{L_{lk}}{C_r}}, \quad \omega_r = \frac{1}{\sqrt{L_{lk}C_r}} \quad (8)$$

The voltage across the leakage inductance L_{lk} is obtained as:

$$V_{lk}(t) = nV_{bat} - v_{cr1}(t_1)\cos\omega_r(t - t_1) \quad (9)$$

In the primary side, the voltage of each transformer had V_{bat} . Thus, the voltage across the switch S_2 was twice V_{bat} and the i_m still increased linearly. The total i_{S1} current is as:

$$i_{S1}(t) = n(i_{lk}(t) + i_m(t)) \quad (10)$$

Mode 3 [t_2, t_3]: At t_2 , the current i_{lk} became zero. Thus, the diode D_1 was turned off at zero current and the reverse recovery losses were removed. Then, voltage across leakage inductance L_{lk} was zero and the voltage across diode D_1 became the reverse voltage of the leakage inductance as follows:

$$V_{D1} = V_d - nV_{bat} \quad (11)$$

The current i_m continues to increase linearly as follows:

$$i_{S1}(t) = ni_m(t) = ni_m(t_2) + \frac{n^2V_{bat}(t - t_2)}{L_m} \quad (12)$$

If magnetizing inductance was sufficiently large, the magnetizing current i_m was almost zero and the switch S_1 could be turned off at zero current.

The analysis of *Modes 4, 5, and 6* is omitted since it is symmetrically repeated during the remaining half switching cycle.

2.2. Design Guidelines

To eliminate the reverse recovery losses of the diode and reduce current stress of the switches, the current i_{lk} decreased to zero before t_3 . From Equation (7), i_{lk} is expressed as follows:

$$i_{lk}(t_2) = I_{lk, peak}\sin\omega_r\Delta t = 0 \quad (13)$$

where Δt is the resonant period as follows:

$$\Delta t = 2\pi\sqrt{L_{lk}\cdot C_r} \quad (14)$$

Since the proposed converter operated in the DCM condition, the resonant period was shorter than the half of T_S . Therefore, the switching frequency f_s should be lower than the resonant frequency f_r as follows:

$$f_s < f_r = \frac{1}{2\pi\sqrt{L_{lk}\cdot C_r}} \quad (15)$$

From Equation (15), the resonant capacitors C_{r1} and C_{r2} can be designed as:

$$C_{r1} + C_{r2} = C_r < \frac{1}{(2\pi f_s)^2 L_{lk}} \quad (16)$$

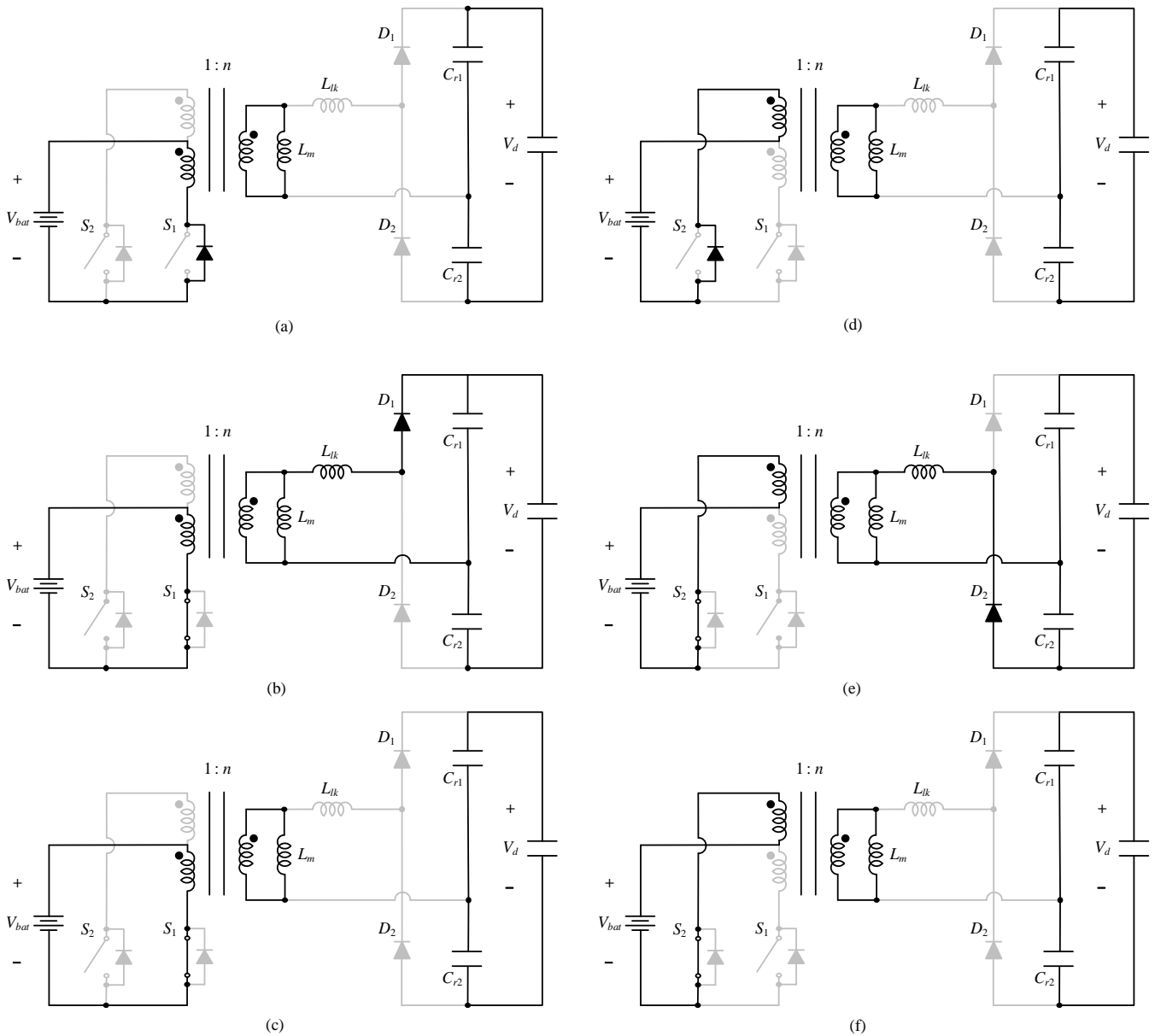


Figure 3. Operation modes: (a) Mode 1; (b) Mode 2; (c) Mode 3; (d) Mode 4; (e) Mode 5; and (f) Mode 6.

In order to reduce the size and the cost of the converter, a high frequency transformer was used in the proposed converter. Figure 5 shows the winding structure of the proposed transformer. The transformer was separately coiled around the primary and secondary windings utilizing a double E core. This method can be used to integrate a resonant inductor and the transformer. The leakage inductance of the transformer constituted the resonant inductor. It was possible to remove the passive component and resonant inductor. Based on the proposed method, the high frequency transformer of the converter was designed.

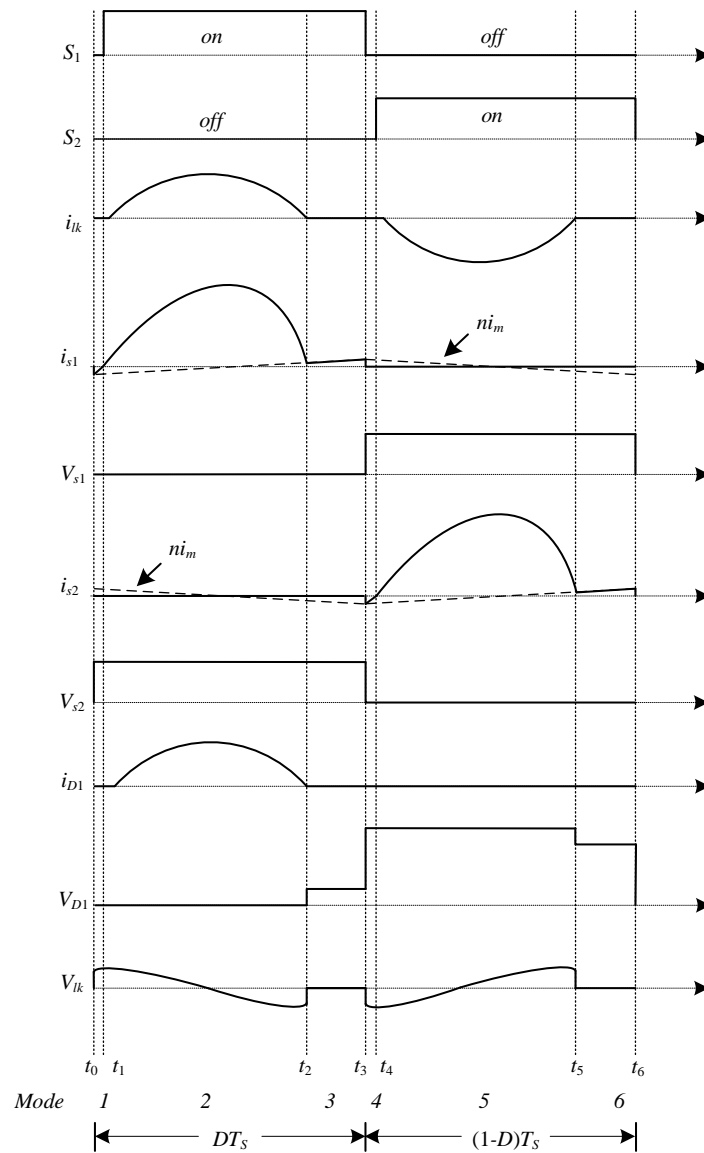


Figure 4. Waveforms of the proposed DC–DC converter according to operating modes of DCM.

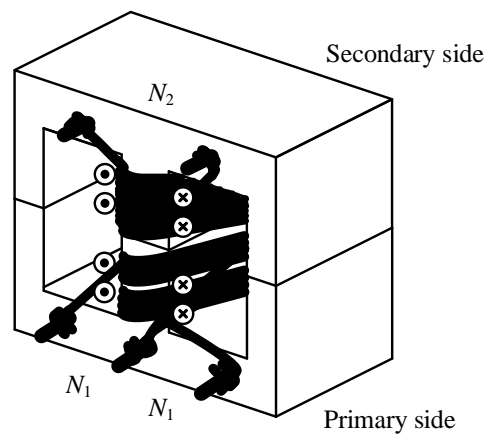


Figure 5. The winding structure for the large leakage inductance.

3. Control Strategy

3.1. Overall System

Figure 6 shows the overall system diagram of the PV standalone converter with the simple controller, which included the entire control. It was realized in low power applications. As shown in Figure 6, the overall system consisted of the synchronous buck converter, the proposed DC–DC converter, and the conventional full-bridge inverter. The synchronous buck converter extracted the power from the panels through the conventional perturb and observe (P&O) MPPT control and charged the battery. The proposed DC–DC converter boosted the low battery voltage to the sufficient voltage to the inverter operation. The conventional full-bridge inverter converted the DC voltage into the sinusoidal AC output voltage.

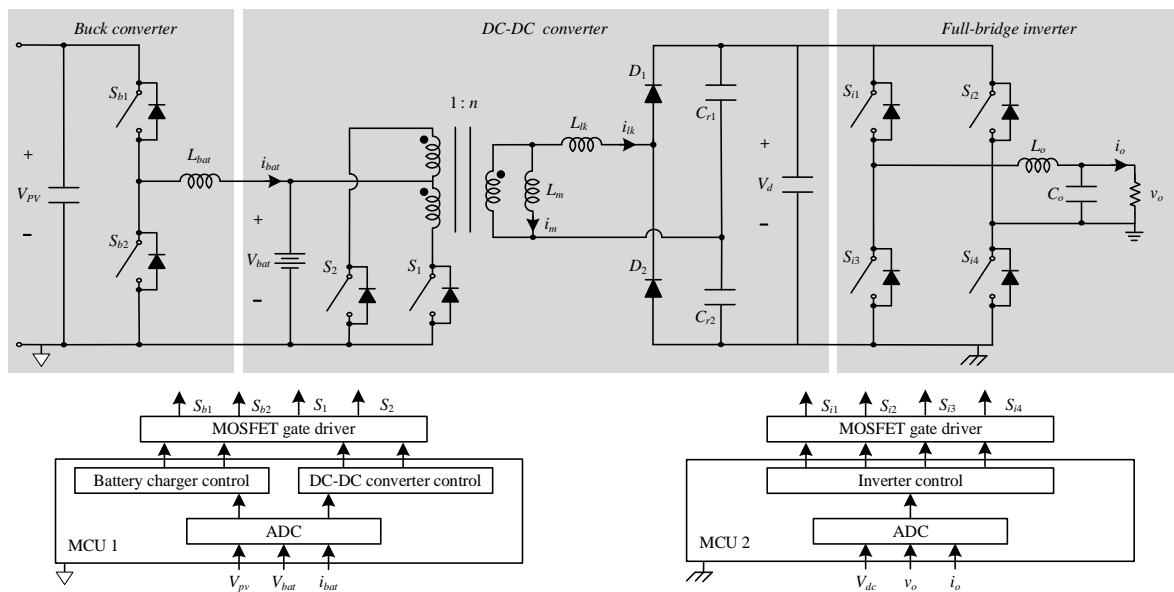


Figure 6. Overall system diagram of the PV standalone converter with the simple controller.

3.2. Control Scheme

To design the control system for the overall standalone PV system with the open loop operation, two independent microcontrollers were used for the primary side and the secondary side. The primary side microcontroller controlled the buck converter and the proposed DC–DC converter. The buck converter performed the conventional P&O MPPT algorithm to extract the maximum power from PV arrays. The proposed DC–DC converter operated with 50% duty of the switching cycle in open loop control. This operation scheme effectively provided the sufficient voltage for the inverter operating without sensing the DC voltage. It had a fast dynamic response and a simple control structure with low-cost implementation. The secondary side microcontroller controlled the conventional full-bridge inverter for its standalone operation. Figure 7 shows the control diagram for the full-bridge inverter. The proposed control design reduced the control complexity and simplified its associated circuit layouts by eliminating the auxiliary circuits for the output voltage feedback control.

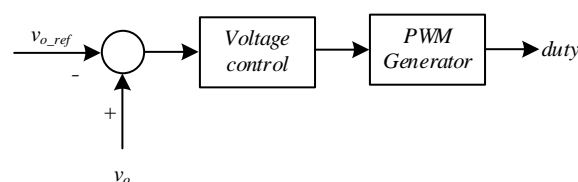


Figure 7. Control diagram for the full-bridge inverter.

4. Experimental Results

To verify the theoretical analysis of the proposed converter for the steady-state condition, the proposed converter was simulated using PSIM 2020a. The major components and parameters are shown in Table 1. Figure 8 shows simulation waveforms in the half load. Figure 8a shows the current and voltage waveforms of the switch S_1 according to the on/off switching states of switches in the one switching cycle. It shows that the current across switch flowed negatively before the on state of the power switch. Thus, the switches were turned on at the zero voltage. Additionally, it shows that the current across switches was reduced by the resonance of the leakage inductance and resonant capacitors before the switch was turned off. Thus, the current stresses across the switches were minimized when the switches were turned off. Figure 8b shows current and voltage waveforms of the diode in the one switching cycle. It shows that the current across the diode decreased to zero. Then, the voltage across leakage inductance became zero and the voltage across the diode became the reverse voltage of the leakage inductance. Thus, the diodes were turned off at the zero current, and the reverse recovery losses were removed.

Table 1. Major components and parameters.

Symbol	Part and Parameters	Value
V_{bat}	Battery voltage	12 V
v_{ac}	AC output voltage	220 V _{rms}
$f_{S,dc}$	Switching frequency (DC–DC converter)	52 kHz
$f_{S,inv}$	Switching frequency (inverter)	17 kHz
1:n	Transformer turns' ratio	1:16
L_{lk}	Leakage inductance	112 μ H
L_m	Magnetizing inductance	1.6 mH
L_o	Output inductance	5 mH
C_{r1}, C_{r2}	Resonant capacitors	47 nF
S_1, S_2	Primary switches (MOSFETs)	IRF2804S
	MOSFET Driver	MIC4427
D_1, D_2	Secondary diodes	16CTU04S,
	Transformer core	EER4950
MCU	Microcontroller	dsPIC33CK32MC105

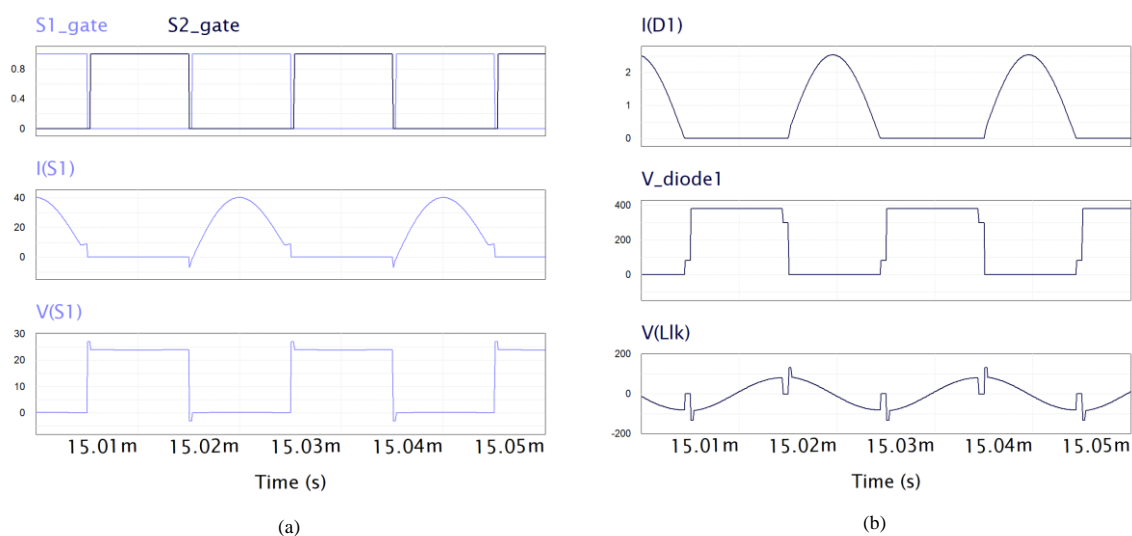


Figure 8. The simulation waveforms: (a) current and voltage waveforms of the switch; (b) current and voltage waveforms of the diode.

To validate the performance of the proposed converter, a 500-W prototype was developed. Figure 9 shows the picture for the experimental step up of the prototype converter.

Figure 10 shows the experimental waveforms of the proposed prototype converter. Figure 10a shows the measured current and voltage waveforms of the switch. The switches were turned off with soft switching at zero voltage and turned on at the minimized current. Figure 10b shows the measured current and voltage waveforms of the diode. Before the diode D_1 was reversely biased, the diode current i_{D1} reached zero and achieved the zero-current turn-off of the diode. After the diode current reached zero, there were parasitic voltage oscillations due to the resonance between stray inductance and capacitance. Figure 11 shows the output current i_o and the output voltage v_o where v_o and i_o are sinusoidal with 60 Hz. Figure 12 shows the power efficiency of the proposed converter at half-load condition according to the battery voltage. The efficiency was 93.1% at battery voltage 12 V.

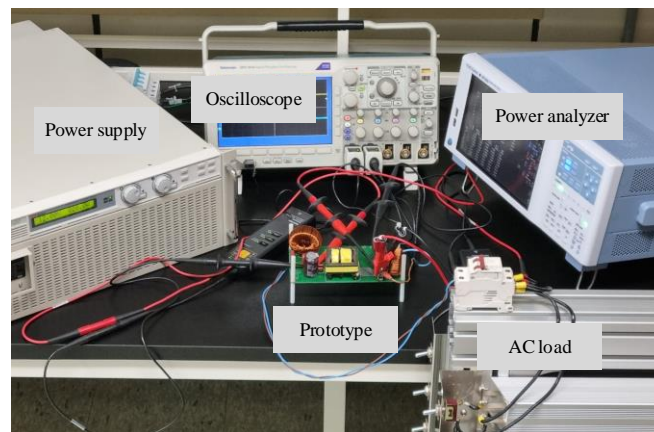


Figure 9. The experimental setup of a 500-W prototype converter.

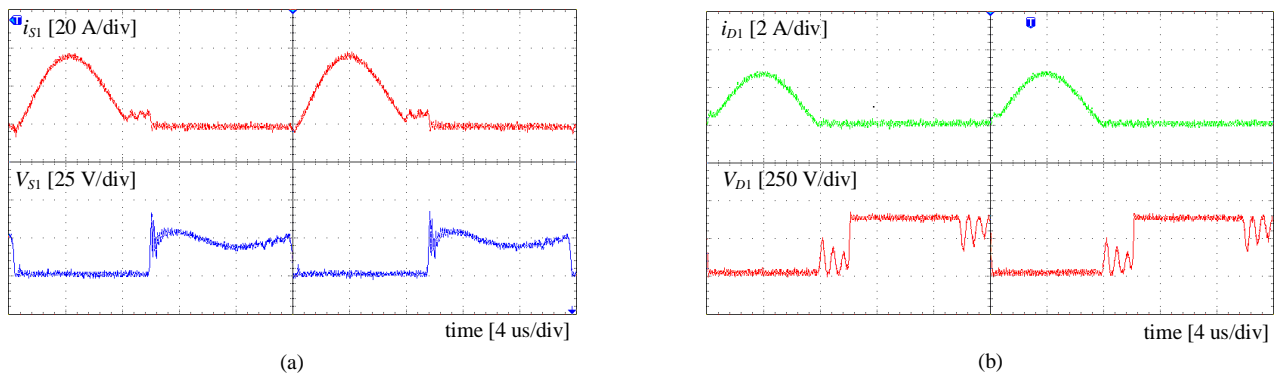


Figure 10. Experimental waveforms: (a) current and voltage waveforms of the switch; (b) current and voltage waveforms of the diode.

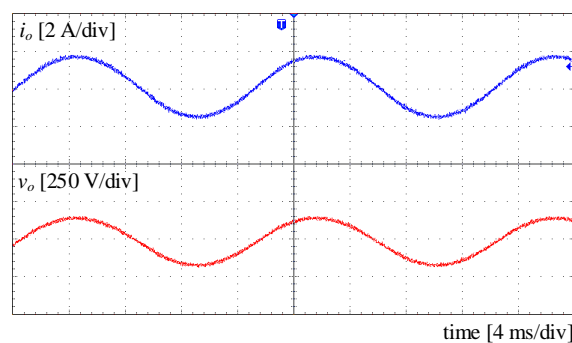


Figure 11. Experimental waveforms: current and voltage waveforms of the output.

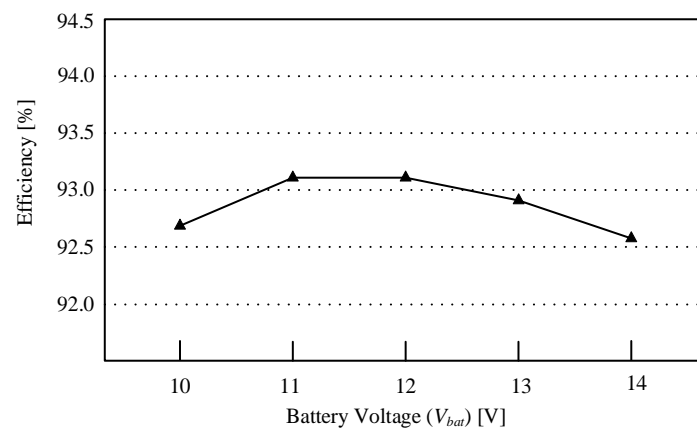


Figure 12. The overall efficiency at half load depending on the charged battery voltage.

5. Concluding Remarks

This paper proposed a step-up DC–DC converter for a power electronic circuit for standalone photovoltaic systems with battery energy storages. The proposed converter operates with soft-switching characteristics in the DCM. The primary switches achieved zero voltage turn on without active clamp circuit or auxiliary circuit to suppress the voltage spike. The secondary diodes achieved zero current turn off. Additionally, the resonant voltage doubler rectifier provided high voltage conversion capability and reduced the high turns' ratio in the transformer with current stress reduction when the primary switches were turned on. Thus, the efficiency increased at minimal components. The control without output voltage control was suggested by using two independent controllers, which simplifies its control design. The overall system configuration and its operation principle were described. The 500-W prototype was experimented at input battery voltage range from 10 to 14 V. It had 93.1% maximum efficiency using 12-V lead-acid batteries.

Author Contributions: Y.-G.O. performed the experiments, analyzed the data, and mainly wrote the manuscript; W.-Y.C. analyzed the experimental data and edited the manuscript; J.-M.K. managed the project and edited the manuscript. All authors have read and agreed to the published version of the manuscript.

Funding: This research was supported by the research fund of Hanbat National University in 2021.

Institutional Review Board Statement: Not applicable.

Informed Consent Statement: Not applicable.

Data Availability Statement: Not applicable.

Conflicts of Interest: The authors declare no potential conflict of interest.

References

1. Pazikadin, A.R.; Rifai, D.; Ali, K.; Mamat, N.H.; Khamsah, N. Design and Implementation of Fuzzy Compensation Scheme for Temperature and Solar Irradiance Wireless Sensor Network (WSN) on Solar Photovoltaic (PV) System. *Sensors* **2020**, *20*, 6744. [[CrossRef](#)] [[PubMed](#)]
2. Wang, W.; Ruan, X. A Modified Reference of an Intermediate Bus Capacitor Voltage-Based Second-Harmonic Current Reduction Method for a Standalone Photovoltaic Power System. *IEEE Trans. Power Electron.* **2016**, *31*, 5562–5573. [[CrossRef](#)]
3. Abbasi, M.; Lam, J. A Step-Up Transformerless, ZV-ZCS High-Gain DC/DC Converter with Output Voltage Regulation Using Modular Step-Up Resonant Cells for DC Grid in Wind Systems. *IEEE J. Emerg. Sel. Top. Power Electron.* **2017**, *5*, 1102–1121. [[CrossRef](#)]
4. Abbasi, M.; Lam, J. A Very High-Gain-Modular Three-Phase AC/DC Soft-Switched Converter Featuring High-Gain ZCS Output Rectifier Modules without Using Step-Up Transformers for a DC Grid in Wind Systems. *IEEE Trans. Ind. Appl.* **2018**, *54*, 3723–3736. [[CrossRef](#)]
5. Kwon, J.M.; Kim, E.H.; Kwon, B.H.; Nam, K.H. High-Efficiency Fuel Cell Power Conditioning System with Input Current Ripple Reduction. *IEEE Trans. Ind. Electron.* **2009**, *56*, 826–834. [[CrossRef](#)]

6. Wu, Q.; Wang, Q.; Xu, J.; Li, H.; Xiao, L. A High-Efficiency Step-Up Current-Fed Push-Pull Quasi-Resonant Converter with Fewer Components for Fuel Cell Application. *IEEE Trans. Ind. Electron.* **2017**, *64*, 6639–6648. [[CrossRef](#)]
7. Piegari, L.; Rizzo, R.; Spina, I.; Tricoli, P. Optimized Adaptive Perturb and Observe Maximum Power Point Tracking Control for Photovoltaic Generation. *Energies* **2015**, *8*, 3418–3436. [[CrossRef](#)]
8. Barros, L.A.M.; Tanta, M.; Sousa, T.J.C.; Afonso, J.L.; Pinto, J.G. New Multifunctional Isolated Microinverter with Integrated Energy Storage System for PV Applications. *Energies* **2020**, *13*, 4016. [[CrossRef](#)]
9. Kwon, J.M.; Kwon, B.H.; Nam, K.H. High-efficiency module-integrated photovoltaic power conditioning system. *IET Power Electron.* **2009**, *2*, 410–420. [[CrossRef](#)]
10. Tran, Y.K.; Freijedo, F.D.; Dujic, D. Open-loop power sharing characteristic of a three-port resonant LLC converter. *CPSS Trans. Power Electron. Appl.* **2019**, *4*, 171–179. [[CrossRef](#)]
11. Li, H.; Jiang, Z. On Automatic Resonant Frequency Tracking in LLC Series Resonant Converter Based on Zero-Current Duration Time of Secondary Diode. *IEEE Trans. Power Electron.* **2016**, *31*, 4956–4962. [[CrossRef](#)]
12. Ma, X.; Wang, P.; Bi, H.; Wang, Z. A Bidirectional LLCL Resonant DC-DC Converter with Reduced Resonant Tank Currents and Reduced Voltage Stress of the Resonant Capacitor. *IEEE Access* **2020**, *8*, 125549–125564. [[CrossRef](#)]
13. Huynh, D.M.; Ito, Y.; Aso, S.; Kato, K.; Teraoka, K. New Concept of the DC-DC Converter Circuit Applied for the Small Capacity Uninterruptible Power Supply. In Proceedings of the 2018 International Power Electronics Conference (IPEC-Niigata 2018-ECCE Asia), Niigata, Japan, 20–24 May 2018; pp. 3086–3091.
14. Wu, Q.; Wang, Q.; Xu, J.; Xiao, L. A Wide Load Range ZVS Push-Pull DC/DC Converter with Active Clamped. *IEEE Trans. Power Electron.* **2017**, *32*, 2865–2875. [[CrossRef](#)]
15. Wu, T.F.; Hung, J.C.; Tsai, J.T.; Tsai, C.T.; Chen, Y.M. An Active-Clamp Push-Pull Converter for Battery Sourcing Applications. *IEEE Trans. Ind. Appl.* **2008**, *44*, 196–204. [[CrossRef](#)]
16. Tarzamni, H.; Babaei, E.; Esmaeelnia, F.P.; Dehghanian, P.; Tohidi, S.; Sharifian, M.B.B. Analysis and Reliability Evaluation of a High Step-Up Soft Switching Push–Pull DC–DC Converter. *IEEE Trans. Reliab.* **2020**, *69*, 1376–1386. [[CrossRef](#)]
17. Wang, Y.; Liu, Q.; Ma, J.; Chen, L.; Ma, H. A New ZVCS Resonant Voltage-fed Push-pull Converter for Vehicle Inverter Application. In Proceedings of the 2013 IEEE International Symposium on Industrial Electronics, Taipei, Taiwan, 28–31 May 2013.
18. Ekkaravarodome, C.; Bilsalam, A.; Tantiviwattanawongsa, P.; Thounthong, P. High Step-Up DC-DC Push-Pull Resonant Based on low Cost half-wave Class-D Rectifier. In Proceedings of the 2019 Research, Invention, and Innovation Congress (RI2C), Bangkok, Thailand, 11–13 December 2019.
19. Ekkaravarodome, C.; Bilsalam, A.; Tantiviwattanawongsa, P.; Thounthong, P. DC-DC High Conversion Ratio Push-Pull Resonant Converter Based on Voltage Double Rectifier. In Proceedings of the 2019 Research, Invention, and Innovation Congress (RI2C), Bangkok, Thailand, 11–13 December 2019.
20. Thippayanet, R.; Ekkaravarodome, C.; Jirasereeamornkul, K.; Chamnongthai, K.; Kazimierczuk, M.K.; Higuchi, K. Push-pull zero-voltage switching resonant DC-DC converter based on half bridge class-DE rectifier. In Proceedings of the 2013 IEEE 10th International Conference on Power Electronics and Drive Systems (PEDS), Kitakyushu, Japan, 22–25 April 2013; pp. 1162–1167.
21. Ekkaravarodome, C.; Sukanna, S.; Bilsalam, A.; Nilphong, S.; Jirasereeamongkul, K.; Higuchi, K. Design of a Balanced Push-Pull Resonant Converter with a Voltage Doubler Class-DE Rectifier. In Proceedings of the 2019 Research, Invention, and Innovation Congress (RI2C), Bangkok, Thailand, 11–13 December 2019.
22. Jia, P.; Mei, Y. Derivation and Analysis of a Secondary-Side LLC Resonant Converter for the High Step-Up Applications. *IEEE J. Emerg. Sel. Top. Power Electron.* **2021**, *9*, 5865–5882. [[CrossRef](#)]